Sinter-crystallisation kinetics of a SiO$_2$–Al$_2$O$_3$–CaO–MgO–SrO glass-ceramic glaze

J.L. Amorós[a,b], E. Blasco[a,*], A. Moreno[a,b], N. Marín[c], C. Feliu[a,b]

[a] *Instituto de Tecnología Cerámica, Asociación de Investigación de las Industrias Cerámicas, Spain*
[b] *Department of Chemical Engineering, Universitat Jaume I, Campus Universitario Riu Sec, 12006 Castellon, Spain*
[c] *Federal University of Sao Carlos, Graduate Program in Materials Science and Engineering, Av. Trab. São Carlense, 400 - Parque Arnold Schimidt, São Carlos, SP, 13566-590, Brazil*

ARTICLE INFO

ABSTRACT

This paper examines the microstructural development and kinetics of the sintering and crystallisation processes of a SiO$_2$–Al$_2$O$_3$–RO (R = Ca, Mg, Sr) glass-ceramic glaze. Crystallisation and sintering kinetics were studied by DTA and HSM, respectively, at different heating rates. The kinetic parameters of crystallisation were determined by the usual methods (Kissinger, Kissinger-Akahira-Sunose, Ozawa and Augis-Bennet methods), and the Johnson–Mehl–Avrami–Kolmogorov (JMAK) model, with an Avrami index of $n = 3$, characteristic of the surface crystallisation of very fine glass particles, was found to describe crystallisation kinetics very well. Sintering could also be described by the JMAK model, but with $n < 1$. Assuming the effect of temperature on the sintering rate to be the same as that of this variable on the inverse of glass matrix viscosity, a model was developed, based on the JMAK model, which only required a single fitting parameter. As the heating rate increased, the degree of overlap between the sintering and crystallisation processes was verified to decrease.

1. Introduction

Two key requirements to obtain glass-ceramics by sinter-crystallisation are the presence of abundant micrometre-sized crystals, obtained mainly by devitrification of frit particles of an appropriate size and composition, and the absence of apparent porosity. Under ideal conditions, sintering of particles ends before crystallisation begins. This yields materials with very low porosity and abundant crystals. However, depending on the glass-ceramic composition and/or thermal cycle used, crystallisation may also begin either before or concurrently with the sintering process, giving rise to inappropriate, porous materials. Unfortunately, it is not easy to formulate frits that, judiciously mixed with 5–10 wt% kaolin, yield a glass-ceramic glaze that, in addition to meeting the above requirements under the typical operating conditions (powder preparation and firing) used in industrial practice, exhibit the desired technical and aesthetic characteristics.

Frits based on the system SiO$_2$–Al$_2$O$_3$–RO (R = Ca, Mg, Zn, Ba, Sr) are widely used in pottery art to obtain good matt glazes [1,2]. Appropriate BaO and/or SrO contents in a frit composition yield almost transparent glazes, in which strong, very pronounced colours with a matt/satin surface can be obtained [1]. Judicious mixing of BaO and/or SrO with other alkaline-earth oxides and ZnO enables glaze surface

properties to be optimised and the firing range increased. According to previous in-house research, this type of frit composition, yielding coatings with good mechanical and aesthetic properties, can be used successfully on an industrial scale, either as porcelain tile glazes or as ink-jet coatings. As no studies were found in the literature on the sinter-crystallisation of this type of SrO-containing glaze, the effect of heating rate and particle size distribution on glaze microstructure and on the kinetics of crystallisation and sintering was investigated. In this paper, only the effect of the heating rate is analysed. The combined effect of this variable and glaze particle size distribution will be studied in a subsequent paper.

1.1. Determination of the kinetic parameters from constant-rate heating experiments

The thermally activated process rate can be described by the equation:

$$\frac{dX}{dt} = k(T)f(X) \tag{1}$$

where f(X) is the kinetic model, which expresses the influence of X (degree of conversion), and k(T) is the rate constant.

* Corresponding author.
  E-mail address: encarna.blasco@itc.uji.es (E. Blasco).

Assuming k(T) follows the Arrhenius equation:

$$k(T) = A\exp\left(-\frac{E}{RT}\right) \tag{2}$$

where A is the pre-exponential factor, E is the process activation energy, and R is the universal gas constant.

For a process at constant-rate heating, a, Eq. (1) and Eq. (2) yield:

$$\frac{dX}{dT} = \frac{A}{a}\exp\left(-\frac{E}{RT}\right)f(X) \tag{3}$$

Separating variables and integrating yields the integral form of the kinetic model, g(X), and its relation to temperature. Using the Murray and White approximation [3] one obtains:

$$g(x) = \int_0^x \frac{dX}{f(X)} = \frac{A}{a}\int_0^T \exp\left(-\frac{E}{RT}\right)dT = \frac{ART^2}{aE}\exp\left(-\frac{E}{RT}\right) \tag{4}$$

Rearranging terms and taking logarithms:

$$\ln\left(\frac{a}{T^2}\right) = \ln\frac{AR}{Eg(X)} - \frac{E}{RT} \tag{5}$$

The following methods were used to determine the kinetic parameters:

i) Kissinger–Akahira–Sunose (KAS) method [4]

Applying the isoconversional principle (i.e. at a constant degree of conversion, X, the process rate, dX/dT, depends only on temperature) to Eq. (5) yields:

$$\ln\left(\frac{a}{T_X^2}\right) = cst - \frac{E_X}{RT_X} \tag{6}$$

Therefore, for each value of X, the value of E_X is determined from the slope obtained on plotting the values of $\ln\left(\frac{a}{T_X^2}\right)$ versus those of $\frac{1}{T_X}$. This is known as the Kissinger–Akahira–Sunose (KAS) method.

i) ii) Kissinger method [5]

On the other hand, applying the mathematical condition of maximum to rate equation Eq. (3), at peak temperature, T_p, one obtains [6]:

$$\frac{Ea}{RT_p^2} + A\left(\frac{df(X)}{dX}\right)_p \exp\left(-\frac{E}{RT_p}\right) = 0 \tag{7}$$

Rearranging terms, taking logarithms, and taking into account that the peak temperature at each heating rate is T_p, yields:

$$\ln\frac{a}{T_p^2} = \ln\left(-\frac{AR}{E}\left(\frac{df(X)}{dX}\right)_p\right) - \frac{E}{RT_p} \tag{8}$$

For many kinetic models, the variation of process degree of progress at peak temperature, X_p, with heating rate, a, may be assumed virtually negligible [7,8]. From Eq. (8), one therefore obtains:

$$\ln\frac{a}{T_p^2} = cst - \frac{E}{RT_p} \tag{9}$$

As a result, plotting $\ln\frac{a}{T_p^2}$ versus $\frac{1}{T_p}$ yields a straight line, whose slope enables determination of process activation energy, E. This is the so-called Kissinger method [5] and the value of the activation energy obtained by this method will hereafter be designated E_K.

i) iii) Johnson–Mehl–Avrami–Kolmogorov (JMAK) model

In order to describe the transformation of a glassy phase into crystals, different kinds of kinetic models, f(X), have been proposed [9–11]. The most widely used model is the Johnson–Mehl–Avrami–Kolmogorov (JMAK) model [12, 13]. This is due to its simplicity, among other

reasons, even though it does not describe the kinetics of this process as well as other more complex models [9–11]. On the other hand, the JMAK model describes glass, glass–zircon composite, and glaze sintering kinetics very well [14–16]. In differential form, the JMAK model [6] is as follows:

$$f(X) = n(1 - X)[-\ln(1 - X)]^{1-1/n} \tag{10}$$

And in integrated form:

$$g(X) = [-\ln(1 - X)]^{1/n} \tag{11}$$

From Eq. (4) and Eq. (11), one obtains:

$$X = 1 - \exp\left\{-\left[\frac{A}{a}\frac{RT^2}{E}\exp\left(-\frac{E}{RT}\right)\right]^n\right\} \tag{12}$$

i) iv) Determination of the Avrami index, n

Rearranging terms and taking logarithms in Eq. (12) yields:

$$\ln[-\ln(1 - X)] = n\ln\left(\frac{ART^2}{aE}\right) - \frac{nE}{RT} \tag{13}$$

In accordance with this expression, if the variation of the first term of the second member is assumed to be negligible compared to that of the second, plotting the pairs of values $(X, T)_a$ obtained at a given heating rate, a, in the form $\ln[-\ln(1-X)]$ versus 1/T, yields a straight line whose slope is directly related to nE [17,18]. Thus, if E is determined by either the KAS or Kissinger method, the Avrami coefficient, n, can be determined from the equation:

$$n = -\left(\frac{R}{E}\right)\frac{\partial[\ln(-\ln(1 - X))]}{\partial(1/T)}\bigg|_a \tag{14}$$

Similarly, based on Eq. (13), plotting the results obtained in experiments at different heating rates, a, but at the same temperature, $(X, a)_T$, in the form $\ln[-\ln(1-X)]$ versus lna, yields a straight line of slope -n. That is:

$$\frac{\partial[\ln(-\ln(1 - X))]}{\partial \ln a}\bigg|_T = -n \tag{15}$$

This is known as the Ozawa method [19].

An alternative way of calculating n is given by the Augis–Bennett equation [20]:

$$n = \frac{2.5/FWHM}{E/RT_p^2} \tag{16}$$

where FWHM is the full width of the crystallisation peak at half maximum in the DTA curve.

Although these methods can be used interchangeably to determine the kinetic parameters (E and n) of both crystallisation (subscript C) and sintering (subscript S), for the latter process, as the direct results of the experiments conducted in the hot stage microscope (HSM) were provided in integrated form, $X_S(T)$, these were studied using the KAS method [4] for the calculation of $E_S(X_S)$ and the Ozawa method [19] (Eq. (15)) and Eq. (14) for that of n_S. Crystallisation was studied by DTA, the Kissinger method being used to calculate the crystallisation activation energy, $E_{C,K}$, and the Augis–Bennett method [20] (Eq. (16)) for the Avrami index, n_C, in addition to the KAS and Ozawa methods. These last two methods required prior calculation of the crystallisation degree of progress from the results in differential form (DTA curve).

2. Material and methods

The study was performed with a commercial frit composition based on the SiO_2–Al_2O_3–CaO–MgO–SrO system (these components make up more than 90 mol% of the frit, Table 1). The frit was obtained by melting the raw materials in an alumina crucible at 1550 °C for 2 h and

Table 1
Nominal composition of the commercial frit (mol%).

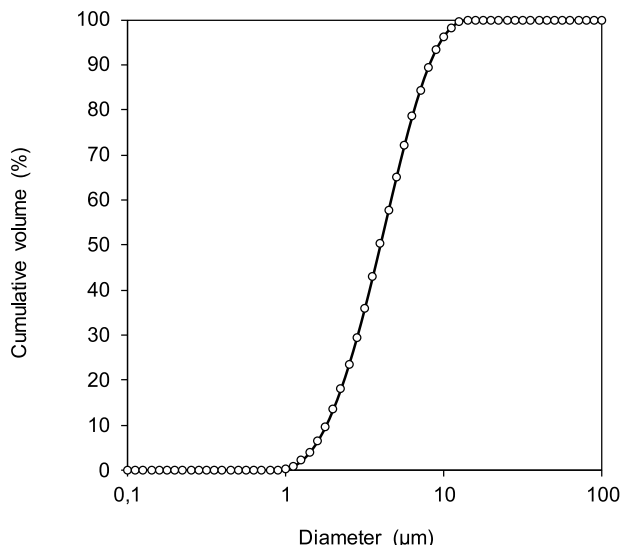| Oxide	SiO$_2$	Al$_2$O$_3$	CaO	MgO	SrO	K$_2$O	ZnO	B$_2$O$_3$	Na$_2$O
mol%	59	13	11	5	5	3	2	1	1

Fig. 1. Particle size distribution of the studied glaze, determined by laser diffraction.

Fig. 2. Development of silhouette axial (ε_h), diametral (ε_d), and surface (ε_A) strains. Experiments at $a = 15$ K/min.

Fig. 3. Method for the determination of X$_c$ (crystallisation degree of conversion) from DTA peak crystallisation. Experimental (squares) and calculated (dashed line) crystallised fraction, X$_c$, as a function of temperature. The calculated values were obtained from the JMAK model with activation energy E$_C$ = 330 KJ/mol, Avrami coefficient n$_C$ = 3, and pre-exponential factor A$_C$ = 4.7·10^{11} s^{-1}. Experiments at $a = 35$ K/min.

the subsequent quenching the resulting melt.

The mixture was prepared by adding 8% kaolin by weight and the usual additives to the frit (0.3% sodium carboxymethylcellulose and 0.1% sodium tripolyphosphate by weight). Aqueous suspensions of the glaze, with a solids volume fraction of 0.65, were wet milled in a laboratory mill until achieving the particle size distribution, PSD, shown in Fig. 1. PSD was determined by laser diffraction (Mastersizer 2000; Malvern Instruments Ltd) using Fraunhofer and Mie theory, respectively, to interpret the light scattering signal collected by the detectors.

Cylindrical test pieces, about 3 mm in diameter and 5 mm in height, were formed by filling a die with powder, compacting with a pressure-gauged push-rod, and extracting the sample onto an alumina plate. The sintering curves were determined from the initial, S$_0$, instantaneous, S, and minimum, S$_{min}$, silhouette surface areas of the test pieces by hot stage microscopy (HSM), at different heating rates ($a = 2$–50 K/min). Diametral, $\varepsilon_d = \ln(d/d_0)$, and axial, $\varepsilon_h = \ln(h/h_0)$, strains were very similar until completion of sintering (Fig. 2). Once the sintering process had been completed, test piece geometry changed, deviating from the cylindrical shape. Thus, assuming isotropic shrinkage, the sintering progress parameter, X, was calculated from:

$$X_S = \frac{\varepsilon_A}{\varepsilon_{A,max}} = \frac{\ln(S_0/S)}{\ln(S_0/S_{min})} \qquad (17)$$

where ε_A and $\varepsilon_{A,\,max}$ are the instantaneous and maximum silhouette surface strain, respectively.

Glass transition temperature, determined by DTA at 5 K/min, was 695 $\pm$ 5 °C and the viscosity assigned was log η_{eff} = 12.3 Pa·s [21]. The fixed viscosity points of the glaze were determined from the shape of the HSM test piece silhouettes, at 5 K/min. The temperatures at which these viscosity points appeared and their assigned values (η_{eff} (Pa·s)) were as follows: initial shrinkage at 810 $\pm$ 5 °C: log η_{eff} = 8.1 $\pm$ 0.1 [22]; maximum shrinkage at 920 $\pm$ 5 °C: log η_{eff} = 6.8 $\pm$ 0.1 [22]; softening at 1220 $\pm$ 5 °C: log η_{eff} = 5.3 $\pm$ 0.1 [22]; half ball at 1245 $\pm$ 5 °C: log η_{eff} = 3.1 $\pm$ 0.1 [22]; and flow at 1265 $\pm$ 5 °C: log η_{eff} = 2.6 $\pm$ 0.1 [22].

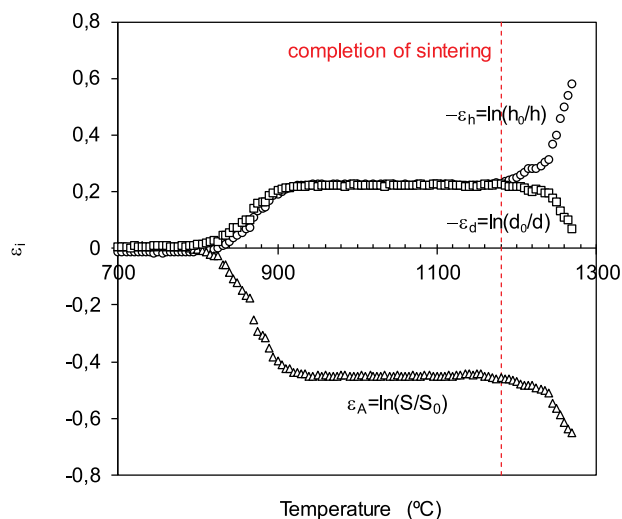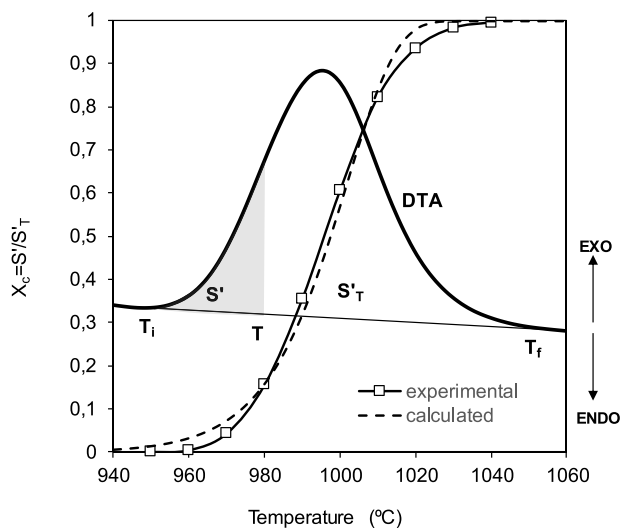To study the crystallisation process, glaze DTA curves were determined at different heating rates ($a = 2$–50 K/min). The DTA curves enabled the crystallisation degree of conversion, X$_C$, to be determined, as shown in Fig. 3. X$_C$, also known as the crystallised fraction, was obtained from the S′/S′$_T$ ratio, where S′ corresponded to the area between T$_i$ (temperature at which crystallisation began) and T, and S′$_T$ was the total area of the crystallisation peak between T$_i$ and T$_f$ (temperature at which crystallisation was completed). Fig. 3 also shows X$_C$ as a function of temperature, determined by this method and calculated from the JMAK model.

To verify that surface crystallisation of the frit was involved and to determine the possible formation of induced crystallisation pores inside the frit particles, frit particles measuring between 1 and 2 mm were prepared. DTA curves were obtained on these frit particles, the frit particles being heat treated at 900 °C for different residence times in a laboratory kiln. The true densities of the starting frit and of the material obtained after complete devitrification (at 900 °C for 24 h) were determined in a helium pycnometer.

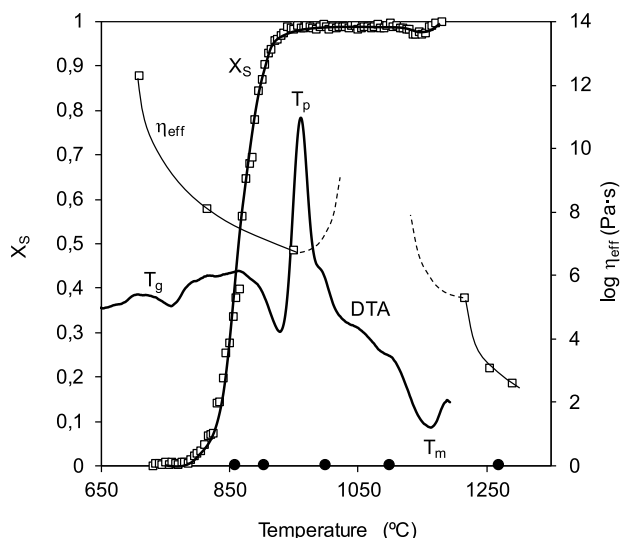Cylindrical test pieces, about 2 cm in diameter and 2 cm in height,

Fig. 4. Sintering, $X_S(T)$, DTA, and effective viscosity, $\eta_{eff}(T)$ (obtained from fixed viscosity points), curves of the glaze at 15 K/min. The solid circles correspond to the temperatures at which the specimens were studied by SEM–EDS.

obtained by slip casting, were subjected to constant-rate heating ($a = 15$ K/min) in a laboratory kiln. These test pieces were characterised by scanning electron microscopy (SEM) and analysed by EDS, at 10 kV and high vacuum. The crystalline phases were identified by X-ray diffraction (XRD).

3. Results

3.1. Behaviour of the glass-ceramic glaze at 15 K/min

The glaze thermogram, Fig. 4, clearly shows the glass transition temperature, T_g, as an inflexion point at $T_g \approx 710°C$; the exothermic crystallisation peak at $T_p \approx 960°C$; and the endothermic melting peak at $T_m \approx 1165°C$. The values of these characteristic temperatures (T_g, T_p, and T_m) varied with the heating rate. XRD showed that the devitrifying phases exhibited diopside and anorthoclase structures (Fig. 5, XRD at 1100°C). T_m was verified to correspond to the diopside melting temperature. Indeed, at temperatures above T_m, diopside was no longer detected (Fig. 5, XRD at 1200°C).

The sintering curve, i.e. the variation of sintering progress parameter, X_S, with temperature, displayed the characteristic sigmoidal shape for most materials with high glassy phase content [14–16]. It shows that densification increased as temperature rose from 800°C, i.e. about 80°C above glass transition temperature, T_g, to frit crystallisation onset at about 940 °C. Above this temperature, the sintering rate decreased progressively until it cancelled out without sintering being completed ($X_S = 0.98$), owing to the increase in the system's effective viscosity, η_{eff}, (dashed line in Fig. 4) as crystallisation advanced [23]. The glaze did not sinter between peak crystallisation temperature ($T_p \approx 960°C$) and melting temperature ($T_m \approx 1165$ °C) because, in this temperature range, crystal content (anorthoclase and diopside) was very high (Figs. 6 and 7). Above T_m, crystals (mainly diopside) began to dissolve in the melt, thus progressively raising glassy phase content and lowering melt viscosity as temperature rose. This led to a decrease in glaze effective viscosity, η_{eff}, which initially gave rise to a slight deformation and swelling of the piece. At higher temperatures, both factors led to a sharp drop in glaze effective viscosity, η_{eff}, (slope of the solid line $\eta_{eff}(T)$).

At low temperatures, with corresponding low X_S values (initial sintering stage), the micrograph of the specimen fired at 860 °C (Figs. 6 and 7) displays the presence of calcined kaolin particles (1) and (2) between spheroidised frit particles (3). Necking onset is solely observed between frit particles that were initially in contact. At temperatures above and below crystallisation temperature, the micrograph of the specimen fired at 905 °C (Figs. 6 and 7) displays high densification of the piece and small light-coloured regions corresponding to reaction areas between frit and calcined kaolin particle surfaces and/or to crystallisation onset, as will be seen below. At temperatures slightly above crystallisation peak temperature ($T_p \approx 960$ °C) (micrograph of the specimen fired at 1000 °C in Fig. 6), crystal content was high and numerous irregularly shaped pores were observed. At 1100 °C (Fig. 6), sintering degree of progress, X_S, was the same as at lower temperatures (1000 °C). However, crystal content was already high (Fig. 7) and crystal size, just as pore size, was larger than at 1000 °C. This growth in pore size and probably in pore volume was related to crystallisation progress. Indeed, if test piece compositional concentration remains constant, an increase in crystal quantity and size, with a greater true density than that of the glassy phase, must lead to a rise in pore volume and size (induced crystallisation pores) [24–26]. At high temperatures (micrograph of the specimen fired at 1270 °C in Figs. 6 and 7), far above melting temperature ($T_m \approx 1165$ °C), crystalline phase content (solely anorthoclase) was lower, crystal size was much larger than at lower
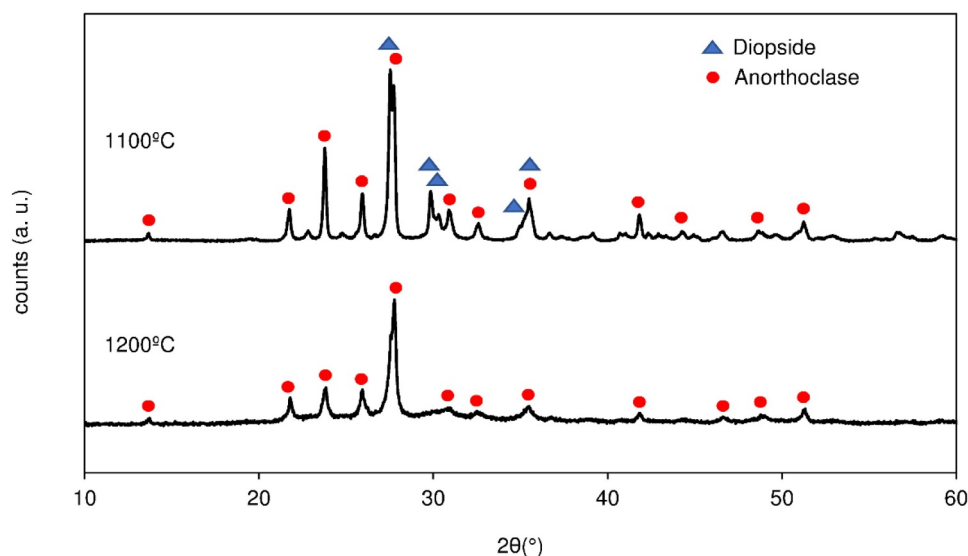

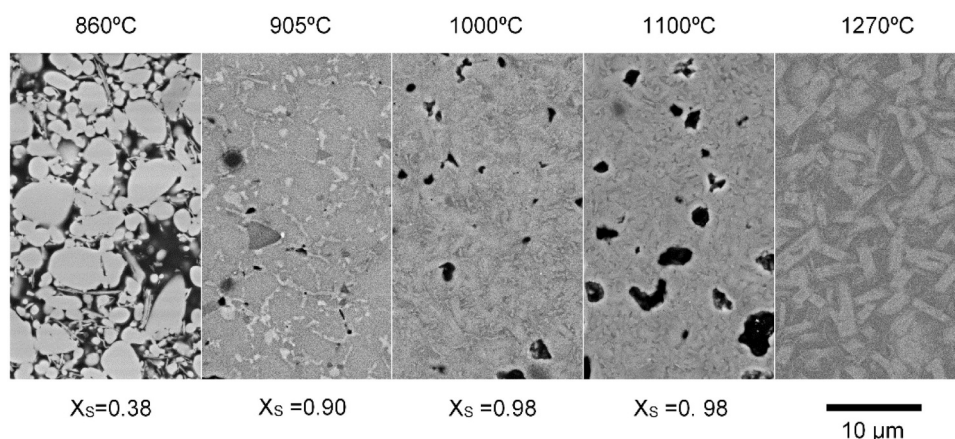**Fig. 5.** XRD of the glaze fired at 1100 °C and 1200°C, at $a = 15$ K/min.

Fig. 6. SEM micrographs of the glaze fired at different temperatures. Heating rate: $a = 15$ K/min.

temperatures, and the test piece was already fully deformed owing to the system's low effective viscosity (intermediate temperature between sphere and flow temperature, Fig. 4).

The comprehensive chemical composition and composition of the crystalline phases present in the test pieces fired at different temperatures were determined by EDS. The most characteristic results are reported in Fig. 7. Comparison of the overall composition with that of the small crystals (4) and (5) in the test piece fired at 905 °C shows that the most important crystal characteristic was a larger SrO content. In contrast, the most characteristic feature of particle (3) was its larger Al_2O_3 and SrO contents and lower proportion of other oxides, also in relation to the overall composition. Particle (6) owed its formation to the reaction between the calcined kaolin and the frit particle surface, as previously assumed.

Abundant contents of two crystalline phases with a different appearance may be observed In the micrograph of the specimen fired at 1100 °C (Fig. 7). The lightest-coloured particles, type (7), were more irregular, their CaO, MgO, and ZnO contents higher, and their Al_2O_3, K_2O, and Na_2O contents lower than those of type (8) particles and of the overall composition. Type (7) particles must correspond to the diopside phase. The other crystalline phase, type (8) particles, consisted of prism-shaped crystals with a greyer shade than that of type (7) particles. Particle (8) Al_2O_3 content was much higher and the SiO_2 and alkali contents lower than those detected in the overall EDS analysis. XRD analysis showed that type (8) particles exhibited an anorthoclase crystalline structure. Finally, small areas of glassy phase (9), with phase separation, may be observed, whose SiO_2, ZnO, K_2O, and Na_2O contents were larger than those of the devitrified crystalline phases. At temperatures above 1160 °C (T_m in the DTA of Fig. 4), only anorthoclase crystals were observed, whose composition changed with temperature. Indeed, their Al_2O_3 and SrO contents increased significantly while they became impoverished in SiO_2, MgO, CaO, and ZnO (crystals (10) and (11) in the micrograph of the specimen fired at 1270 °C in Fig. 7). At these temperatures, the CaO, MgO, ZnO, and SiO_2 contents in the glassy phase (12) were larger than those detected overall.

3.2. Crystallisation of the glass-ceramic glaze

Surface crystallisation was confirmed by SEM microscopy, using polished specimens of 1–2 mm frit particles fired at 900 °C for different residence times (Fig. 8). Indeed, every micrograph shows column-shaped crystals growing at right angles to frit particle surfaces. Crystal size and crystal layer thickness grew with residence time. At 24 h, particle crystallisation had already been completed.

Fig. 9 shows an induced crystallisation pore in the middle of a frit particle, as the density of the fully crystallised specimen (2.91 ± 0.01 g/cm³) was greater than that of the starting frit

(2.67 ± 0.01 g/cm³). The columnar dendritic crystals (anorthoclase) grew from the surface towards the centre, in whose proximity they became smaller and more isometric. The diopside crystals appeared as small bright particles next to the anorthoclase crystals. The microstructure of the frit particles (1–2 mm in size) that had devitrified by surface crystallisation thus exhibited column-shaped crystals larger than 30 μm and induced crystallisation pores of the same order of magnitude as that of the particle, in contrast to what occurred in the glaze fired at the usual temperature, with much smaller, more isometric crystals (micrograph of the glaze fired at 1100 °C in Fig. 7) and also much smaller intergranular and induced crystallisation pores (micrograph of the glaze fired at 1100 °C in Fig. 6).

The DTA curves of the glaze at different heating rates and of the large frit particles (1–2 mm) at 25 K/min are shown in Fig. 10. The crystallisation temperature (maximum in the exothermic peak), T_p, clearly shifted to higher values when the heating rate, a, increased. The effect of the heating rate, a, on the transition, T_g, and melting, T_m, temperatures was smaller than on the crystallisation temperature, T_p, (Fig. 11). In every case, these temperatures increased as the logarithm of the heating rate, a, increased. The DTA curves obtained at 25 K/min (for the glaze and the large frit particles (1–2 mm)) (Fig. 10) confirmed that the crystallisation temperature of the coarsest specimen (1–2 mm) was more than 200 °C higher and the peak was broader and more asymmetric than that of the composition. Such behaviour is characteristic of glass surface crystallisation [26,27].

3.2.1. Kinetic analysis

The DTA curves of the composition at different heating rates ($a = 2$, 5, 10, 15, 25, 35, and 50 K/min) were used to determine the corresponding crystallisation peak temperatures, T_p. In accordance with Eq. (9) (Kissinger method), $E_{C,K}$ was calculated from the slope of the linear fitting of $\ln\frac{a}{T_p^2}$ versus $\frac{1}{T_p}$ (Fig. 12), $E_{C,K}$ being 327 ± 6 kJ/mol.

In order to obtain $E_C(X_C)$ by the KAS method, the crystallisation curves of the glaze, $X_C(T)$, at different heating rates, a, were obtained from the DTA curves by the method described in Section 2 (Fig. 3). In accordance with Eq. (6), plots of $\ln(\frac{a}{T_X^2})$ versus $\frac{1}{T_X}$ at different X_C were made (Fig. 13). In every case, straight lines were obtained and the $E_C(X_C)$ values were determined from the fitting lines. The results of $E_C(X_C)$ as a function of the crystallised fraction, X_C, for the glaze are shown in Fig. 14. A clearly decreasing trend in $E_C(X_C)$ with rising X_C was observed, as also reported by other researchers [9, 11]. However, $E_C(X_C)$ was practically constant in the $0.3 \leq X \leq 0.7$ range ($\overline{E_C(X)} = 324 \pm 9$ kJ/mol), which practically coincided with the values obtained by the Kissinger method ($E_{C,K} = 327 \pm 6$ kJ/mol).

The values of the Avrami parameter, n_C, calculated by different methods from the DTA curves at different heating rates, a, are detailed in Table 2. The values of n_C calculated by the Augis–Bennett method
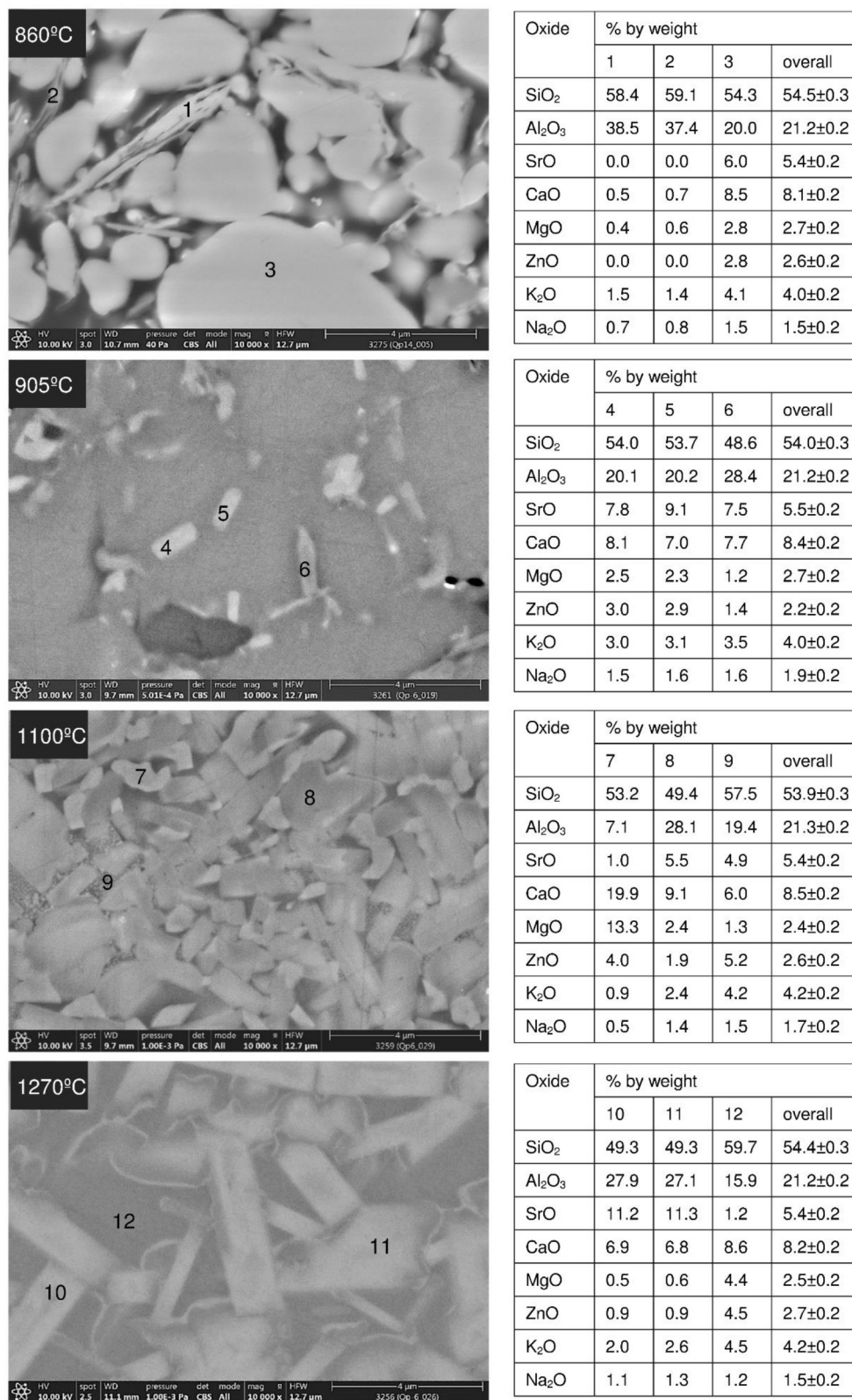
Oxide	% by weight			
	1	2	3	overall
SiO₂	58.4	59.1	54.3	54.5±0.3
Al₂O₃	38.5	37.4	20.0	21.2±0.2
SrO	0.0	0.0	6.0	5.4±0.2
CaO	0.5	0.7	8.5	8.1±0.2
MgO	0.4	0.6	2.8	2.7±0.2
ZnO	0.0	0.0	2.8	2.6±0.2
K₂O	1.5	1.4	4.1	4.0±0.2
Na₂O	0.7	0.8	1.5	1.5±0.2

Oxide	% by weight			
	4	5	6	overall
SiO₂	54.0	53.7	48.6	54.0±0.3
Al₂O₃	20.1	20.2	28.4	21.2±0.2
SrO	7.8	9.1	7.5	5.5±0.2
CaO	8.1	7.0	7.7	8.4±0.2
MgO	2.5	2.3	1.2	2.7±0.2
ZnO	3.0	2.9	1.4	2.2±0.2
K₂O	3.0	3.1	3.5	4.0±0.2
Na₂O	1.5	1.6	1.6	1.9±0.2

Oxide	% by weight			
	7	8	9	overall
SiO₂	53.2	49.4	57.5	53.9±0.3
Al₂O₃	7.1	28.1	19.4	21.3±0.2
SrO	1.0	5.5	4.9	5.4±0.2
CaO	19.9	9.1	6.0	8.5±0.2
MgO	13.3	2.4	1.3	2.4±0.2
ZnO	4.0	1.9	5.2	2.6±0.2
K₂O	0.9	2.4	4.2	4.2±0.2
Na₂O	0.5	1.4	1.5	1.7±0.2

Oxide	% by weight			
	10	11	12	overall
SiO₂	49.3	49.3	59.7	54.4±0.3
Al₂O₃	27.9	27.1	15.9	21.2±0.2
SrO	11.2	11.3	1.2	5.4±0.2
CaO	6.9	6.8	8.6	8.2±0.2
MgO	0.5	0.6	4.4	2.5±0.2
ZnO	0.9	0.9	4.5	2.7±0.2
K₂O	2.0	2.6	4.5	4.2±0.2
Na₂O	1.1	1.3	1.2	1.5±0.2

Fig. 7. SEM micrographs and phase compositions determined by EDS of the glaze fired at different temperatures. Heating rate: $a = 15$ K/min. The uncertainly of overall EDS analysis was the standard deviation of 12 measurements, 3 for each temperature.

(Eq. (16)) and by Eq. (14), using the Kissinger value, $E_{C,K}$, or the average value obtained by the KAS method, $\overline{E_C(X)}$, for the crystallisation activation energy, at each heating rate, a, were very similar. In addition, n_C was generally observed to decrease as the heating rate, a, increased, as also reported elsewhere [9]. Analogously, the values of n_C resulting from averaging the value obtained at each heating rate, a, coincided for these two methods and also coincided with the value determined by the Ozawa method. A value of n_C close to 3 was found to
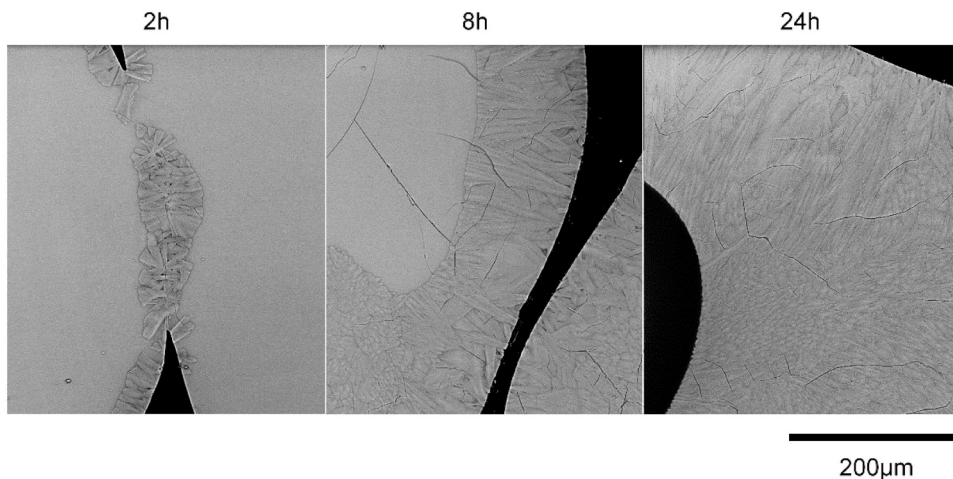
Fig. 8. SEM micrographs of 1–2 mm frit particles fired at 900 ºC for different times.
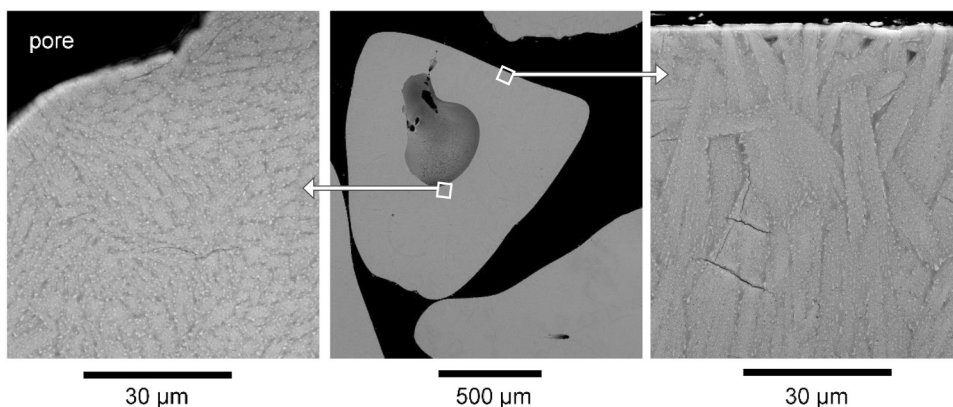

Fig. 9. SEM micrographs of the surface and interior of 1–2 mm frit particles fired at 900 ºC for 24 h.
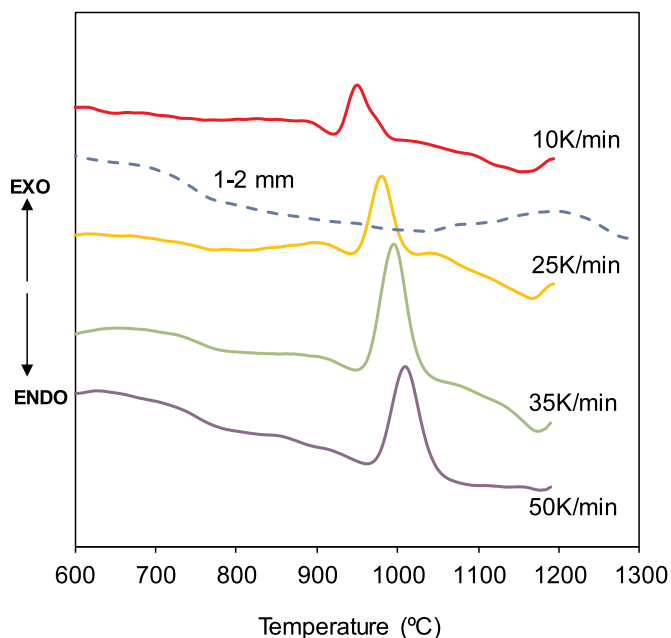

Fig. 10. DTA curves of the glaze at different heating rates and of large frit particles (1–2 mm) at 25 K/min.

correspond to the surface crystallisation of very small frit particles. Indeed, as reported in various studies [26,28,29], the induced surface crystallisation of fine grained glass led to the formation of not very anisometric crystals (Fig. 7, specimen fired at 1100 ˚C), with a corresponding value of n_C close to 3. In contrast, in the induced surface crystallisation of bulk glass, the coarse particles gave rise to highly anisometric crystals (Fig. 9) and hence to values of n_C close to 1.

For every test heating rate, a, the results obtained from the crystallisation curves $X_C(T)$, i.e. the values (X_C, T, a), were fitted to Eq. (12) by non-linear regression, minimising the difference between the experimentally obtained values of X_C, $X_{C,exp}$, and the values calculated from the model, $X_{C,cal}$, by the least squares method. The residual sum of squares (RSS) was minimised in the form:

$$RSS= \sum (X_{C,exp} - X_{C,cal})^2 = min \qquad (18)$$

The RSS obtained was converted to the variance, S^2, as follows:

$$S^2 = \frac{RSS}{m - p} \qquad (19)$$

where m is the total number of experimental points used in the calculation and p is the number of kinetic parameters obtained on applying the model.

The results fitted Eq. (12) quite well, particularly in the range of values $0.2 \leq X_C \leq 0.8$, as may be observed in Figs. 3 and 18. The values of the kinetic triplet were as follows: $E_C = 330$ KJ/mol, $n_C = 3$,
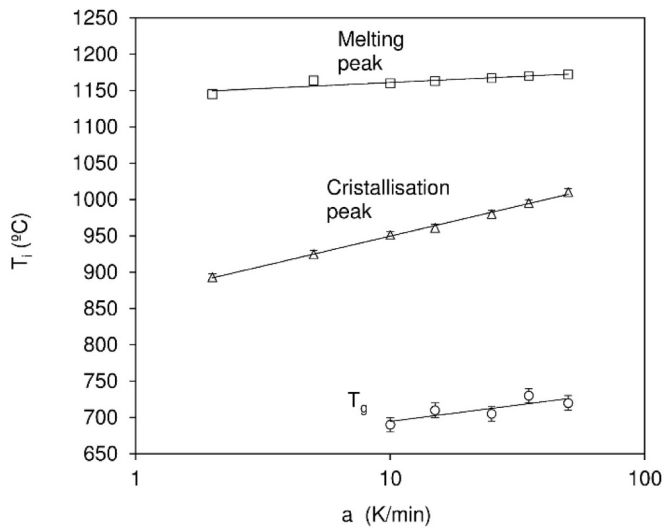
Fig. 11. Effect of heating rate, a, on melting peak, T_m, crystallisation peak, T_p, and glass transition, T_g, temperatures (DTA) of the glaze. The error bars are the standard deviation of values.
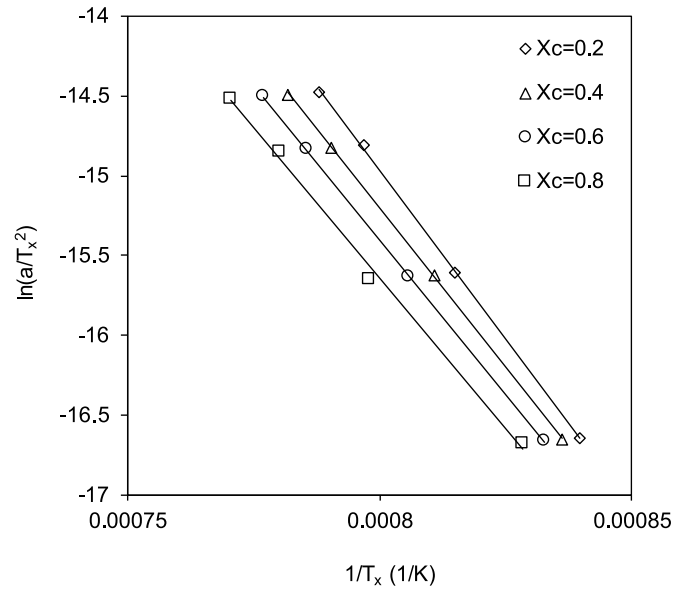

Fig. 13. KAS plot of the glaze (Eq. (6)) at different crystallised fractions, X_C.
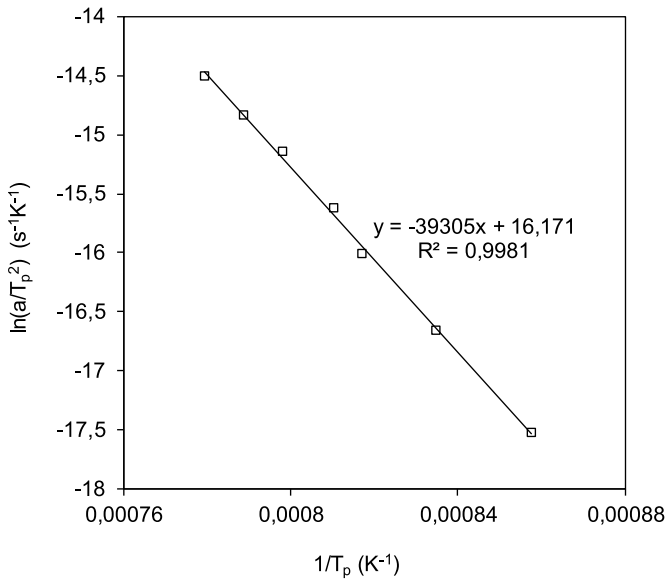

Fig. 12. Kissinger plot of the glaze (Eq. (9)).

Fig. 14. Crystallisation activation energy, $E_C(X_C)$, obtained by the KAS method, as a function of the crystallised fraction, X_C. The error bars correspond to the standard error of the slope to the linear fitting: $\ln(\frac{a}{T_X^2})$ versus $\frac{1}{T_X}$ at different crystallised fractions, X_C, (Fig. 12). $E_{C,K}$ is the crystallisation activation energy obtained by the Kissinger method.

and $A_C = 4.7 \cdot 10^{11}$ s^{-1}, the variance, S^2, being $1.8 \cdot 10^{-3}$. The first two values practically coincided with those obtained by other methods.

3.3. Sintering of the glass-ceramic glaze

The effect of the heating rate, a, on the sintering curves, $X_S(T)$, (Fig. 15) was verified largely to depend on the influence of this variable on glaze crystallisation (Figs. 10 and 11). Indeed, at the lowest test heating rate ($a = 2$ K/min), sintering began at a lower temperature than at the other rates. However, as crystallisation also started at lower temperatures, temporary sintering halt (practically horizontal segment of curve $X_S(T)$ in Fig. 15) similarly occurred at lower temperatures, with an analogously lower sintering degree of conversion, $(X_S)_p$. It may further be observed that this section of the sintering curve, corresponding to densification arrest, became smaller as the heating rate, a, increased until it disappeared at rates above 15 K/min. This behaviour had already been observed in this type of material [15,23].
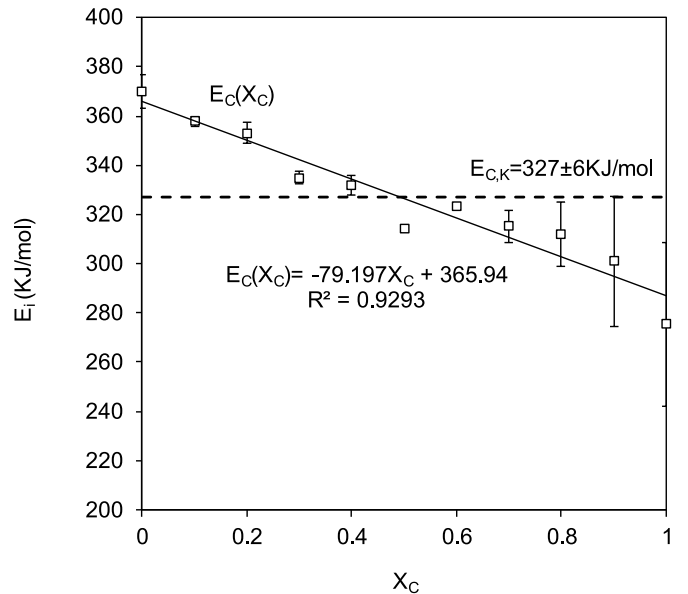
3.3.1. Kinetic analysis

Pairs of values (a, T_X) were obtained from the experimental sintering curves (Fig. 15) for different values of X_S and plotted, in accordance with Eq. (6), in the form $\ln(\frac{a}{T_X^2})$ versus $\frac{1}{T_X}$ (KAS method) (typical plots are shown by way of example in Fig. 13). In every case, good linear fits were obtained from which the values of the sintering activation energy, $E_S(X_S)$, were calculated for different sintering degrees of progress, X_S (Fig. 16). The values of $E_S(X_S)$, albeit scattered, decreased linearly as sintering degree of progress, X_S, increased. This behaviour, which was similar to that of crystallisation activation energy, must be due to viscous flow activation energy also decreasing as temperature rose [14,30].

With a view to verifying this assumption, the viscosity curve corresponding to a glass matrix of the same composition as that of the test

Table 2
Values of the Avrami parameter, n_C, obtained by different methods.

a (K/min)	Augis–Bennett (Eq. (16)) [20]	Ozawa (Eq. (15)) [19] *	Eq. (14) ** $E_{C,K} = 327 \pm 6$ kJ/mol	$\overline{E_C(X)} = 324 \pm 9$ kJ/mol
5	3.4		3.3 ± 0.2	3.4 ± 0.2
10	3.2		3.1 ± 0.3	3.2 ± 0.3
15	3.5	3.1 ± 0.5	3.1 ± 0.5	3.1 ± 0.5
35	2.8		3.0 ± 0.3	3.0 ± 0.3
50	2.7		2.9 ± 0.3	2.9 ± 0.3
Average	3.1 ± 0.4	3.1 ± 0.5	3.1 ± 0.1	3.1 ± 0.2

* The uncertainty of n was the standard error of the slope to the linear fitting: $\ln(-\ln(1-X_C)$ versus $-\ln a$, at T = 975 °C.

** The uncertainty of n was the standard error of the slope to the linear fitting: $\ln(-\ln(1-X_C)$ versus $1/T$, at different heating rates, a.
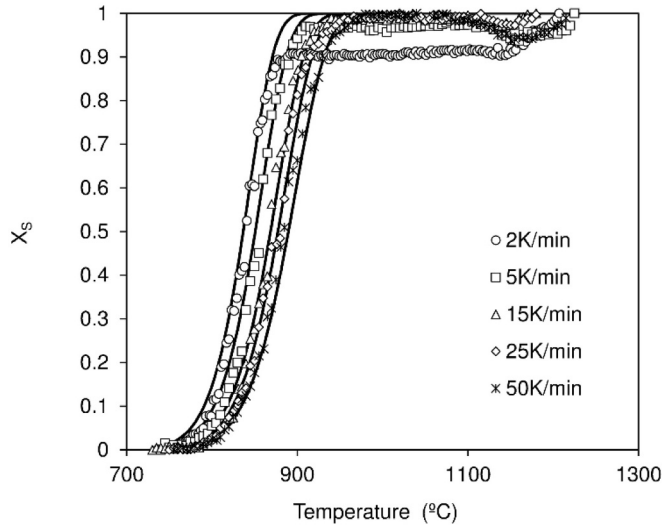

Fig. 15. Effect of heating rate, a, on the sintering curves, X_S vs T. The symbols are experimental data and the solid lines correspond to the values calculated from the model (Eq. (21)).
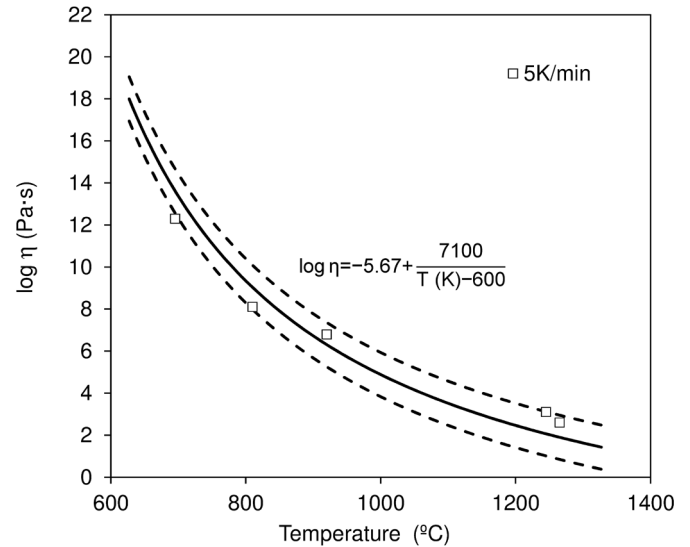

Fig. 17. Estimated viscosity–temperature curve of a glass matrix with the same composition as the glaze, fitted to the Vogel–Fucher–Tamman (VFT) equation. The dashed lines represent the standard deviation of the $\log \eta$ values. The fixed viscosity points were obtained at 5 K/min by HSM.
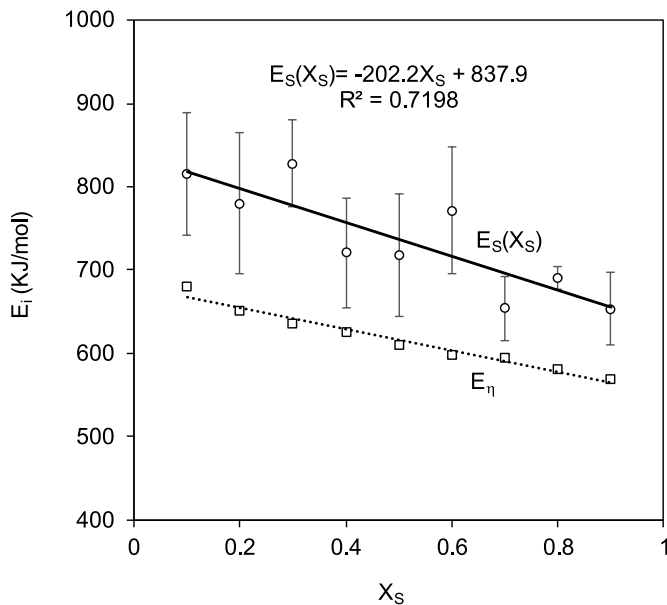

Fig. 16. Sintering activation energy, $E_S(X_S)$, obtained by the KAS method, and viscous flow activation energy, E_η, as a function of the sintered fraction, X_S. The error bars are the standard error of the slope to the linear fitting: $\ln(\frac{a}{T_X^2})$ versus $\frac{1}{T_X}$ at different sintering degrees of progress, X_S, (Fig. 12).

glaze was estimated, from that curve then calculating the values of the viscous flow activation energy, $E_\eta(X_S)$. To do so, first, the fixed viscosity points of the glaze, obtained at 5 K/min, were assumed to be practically independent of crystalline phase content, except for the softening point. As the crystallised fraction was small, the maximum shrinkage point was therefore assumed practically to correspond to that of the glass matrix. It was analogously assumed that glass matrix viscosity in the glaze at the temperatures corresponding to the half-ball and flow points was so low that the presence of crystals, presumably not very abundant, hardly affected system viscosity. In any event, the real viscosity of the glass matrix corresponding to these two fixed viscosity points must be a little lower than the estimated viscosity owing to the presence of crystalline phase. Taking into account these considerations, the fixed viscosity points were fitted to the Vogel–Fulcher–Tamman (VFT) equation (Fig. 17). The values of viscous flow activation energy, Eη(X_S), for different values of X_S, and therefore for different temperature ranges were calculated by fitting the pairs of values: estimated viscosity–temperature for the range of temperatures considered to the Arrhenius equation. These results, $E_\eta(X_S)$, are included in Fig. 16. It may be observed that, as expected, the decrease in $E_S(X_S)$ with X_S was similar to that of $E_\eta(X_S)$ with X_S.

The n_S values were calculated by the Ozawa method (Eq. (15)). To do so, at each selected temperature, the pairs of values (X_S, a) were determined from the sintering curve X_S(T) (Fig. 15) and plotted in the form $\ln[-\ln(1-X)]$ versus $-\ln a$. For every temperature, the results were fitted to straight lines from which the values of n_S were obtained (Table 3). The average value of the Avrami parameter, $\overline{n_S}$, was

Table 3

Values of Avrami parameter, n_S, of sintering obtained at different temperatures and average $\overline{n_S}$ (Ozawa method).

T (°C)	800	810	820	830	840	850	860	870	$\overline{n_S}$**
n_S*	0.49 ± 0.07	0.55 ± 0.12	0.58 ± 0.09	0.55 ± 0.07	0.59 ± 0.02	0.56 ± 0.03	0.56 ± 0.05	0.56 ± 0.03	0.56 ± 0.03

  * The uncertainty of n_S was the standard error of the slope to the linear fitting: $\ln(-\ln(1-X_S))$ versus $-\ln a$, at different temperatures.

  ** The uncertainty of $\overline{n_S}$ was the standard deviation of n_s values.

Table 4

Values of the kinetic parameters, obtained on fitting the experimental sintering points to Eq. (12), and variance of the fits, S^2, calculated by Eq. (18) and Eq. (19).

a (K/min)	E_S (KJ/mol)	$\overline{n_S}$	A_S (s^{-1})	S^2
2	800	0.56	$4.84 \cdot 10^{34}$	$2.6 \cdot 10^{-3}$
5	755	0.56	$2.67 \cdot 10^{32}$	$7.3 \cdot 10^{-4}$
15	685	0.56	$1.75 \cdot 10^{29}$	$5.4 \cdot 10^{-4}$
25	660	0.56	$1.27 \cdot 10^{28}$	$6.2 \cdot 10^{-4}$
50	614	0.56	$1.17 \cdot 10^{26}$	$5.2 \cdot 10^{-4}$
Overall fit	700	0.56	$8.60 \cdot 10^{29}$	$1.1 \cdot 10^{-3}$

consistent with the values obtained in the sintering of glass–zircon composites [14,31]. In those studies, it was verified that the JMAK model appropriately described the sintering process of these materials with values of n_S that decreased from $n = 0.7$ for the glass, used as matrix, to $n_S \approx 0.4$, as the rigid particle (zircon) volume fraction increased and the ratio: rigid particle size/glass matrix size decreased.

The pairs of values (X_S, T) of the sintering curves obtained at different heating rates, a, and at temperatures below glaze crystallisation onset (sintering arrest) were fitted to Eq. (12) by non-linear regression (Eq. (18)), taking $\overline{n_S} = 0.56$ as fixed parameter. The results are detailed in Table 4. It may be observed that, as heating rate, a, increased, sintering activation energy, E_S, decreased, as the range of temperatures in which sintering developed shifted towards higher temperatures (Fig. 15). This behaviour resembled that which occurred with the variation of $E_S(X_S)$ with X_S (Fig. 16) and of $E_\eta(X_S)$ with X_S. Finally, the sintering results obtained at every heating rate were fitted to Eq. (12). The values obtained for the parameters are also included in Table 4.

In view of these results, the effect of temperature on the rate constant, k(T), was assumed to be due to the influence of this variable on the inverse of glass matrix viscosity, as reported elsewhere [14,31]. It can therefore be described by an expression, based on a VFT-type viscosity equation, of the form:

$$k(T) = A^* \cdot \exp\left(-\frac{B}{T-T_0}\right) \tag{20}$$

where $B = 7100$ K and $T_0 = 600$ K are the values of the VFT equation parameters for viscosity of the glass matrix and A^* is the pre-exponential factor.

Substituting Eq. (20) for Eq. (2) and operating analogously to the form described in Section 1.1 yields:

$$X_S = 1 - \exp\left\{ -\left[\frac{A^*}{a} \frac{(T-T_0)^2}{B} \exp\left(-\frac{B}{(T-T_0)}\right) \right]^n \right\} \tag{21}$$

Using non-linear regression (Eq. (18)) to fit the sintering results to Eq. (21), keeping $n = 0.56$ constant and introducing the above values of B and T_0, yielded values of $A^* = 9.50 \cdot 10^{10}$ s^{-1} and $S^2 = 1.43 \cdot 10^{-3}$. Although only one fitting parameter was used, the value of S^2 was similar to that obtained in the overall fit of Table 4, in which two parameters were required. As may be observed in Fig. 15 and Fig. 18, the agreement between the experimental data and the calculated values was very good.

3.4. The competition between sintering and crystallisation: effect of heating rate, a

Fig. 18 shows the plots, at heating rates of $a = 5$, 15, and 50 K/min, of the calculated sintering, $X_S(T)$, and crystallisation, $X_C(T)$, curves together with the corresponding experimental points. The crystallisation curve was calculated from Eq. (12), using as parameters the values: $n_C = 3$, $E_C = 330$ KJ/mol, and $A_C = 4.7 \cdot 10^{11}$ s^{-1}. The sintering curves were calculated from Eq. (12) and Eq. (21), for the former using the values detailed in the overall fit of Table 4 (black line) and for the latter using $B = 7100$ K and $T_0 = 600$ K of the VFT viscosity equation and $A^* = 9.50 \cdot 10^{10}$ s^{-1} (red line). The vertical dashed straight line indicates the temperature at which glass-ceramic glaze crystallisation began and was calculated, according to the model, as the temperature at which the degree of crystallisation was $X_C = 0.01$. Examination of this figure reveals the following:

i) As the heating rate, a, rose, sintering and crystallisation both developed at increasingly higher temperatures. However, the effect of "a" on the shift in temperature range in which crystallisation developed was much greater than that on the shift in sintering temperature range, i.e. the two curves separated. The overlap of the two processes therefore decreased as "a" rose: at the highest test "a" (i.e. 50 K/min), crystallisation began when sintering had already been completed, whereas at low "a" (5 K/min), crystallisation began when sintering had not yet ended.

ii) The sintering curve obtained from the model described by Eq. (21), based on the effect of temperature on the rate constant being the same as that of this variable on the inverse of glass matrix viscosity (of the VFT-type equation), fitted better to the experimental data at high sintering degrees of progress, X_S, than that described by Eq. (12).

iii) Generally speaking, the developed models, which describe glaze sintering and crystallisation, appropriately determined the degree of sintering at which shrinkage halted, $(X_S)_p$, and the critical degree of crystallisation, $(X_C)_p$, at which this occurred, as a function of the heating rate, a.

In regard to the last point (iii), with a view to drawing more general conclusions, the degree of crystallisation at which sintering halted, $(X_C)_p$, was assumed to be independent of the thermal variables. That is, the thickness of the crystal shell that formed at the particle surface where sintering halted was assumed to depend on frit particle size distribution and nature and not on process kinetics. In this case, the models used, with the appropriate kinetic parameters for each glaze, enabled the sintering degree of progress when sintering halted, $(X_S)_p$, to be calculated as a function of the heating rate, a, as the critical crystallisation fraction, $(X_C)_p$, had already been reached in the glaze. To do so, in the particular case of this glaze, the pairs of values (T, a) at which an assumed critical degree of crystallisation, $(X_C)_p$, was reached were determined from the crystallisation model (Eq. (12)). These pairs of values allowed the degree of sintering attained, $(X_S)_p$, to be calculated from Eq. (21). The calculated curves: $(X_S)_p$ vs a, at $(X_C)_p = 0.05$ and $(X_C)_p = 0.1$ are plotted as dashed lines in Fig. 19. It may be observed that, as the heating rate, a, rose, glaze degree of sintering, $(X_S)_p$, at a given critical degree of crystallisation, $(X_C)_p$, increased. These curves shifted towards lower values of $(X_S)_p$ as the critical degree of
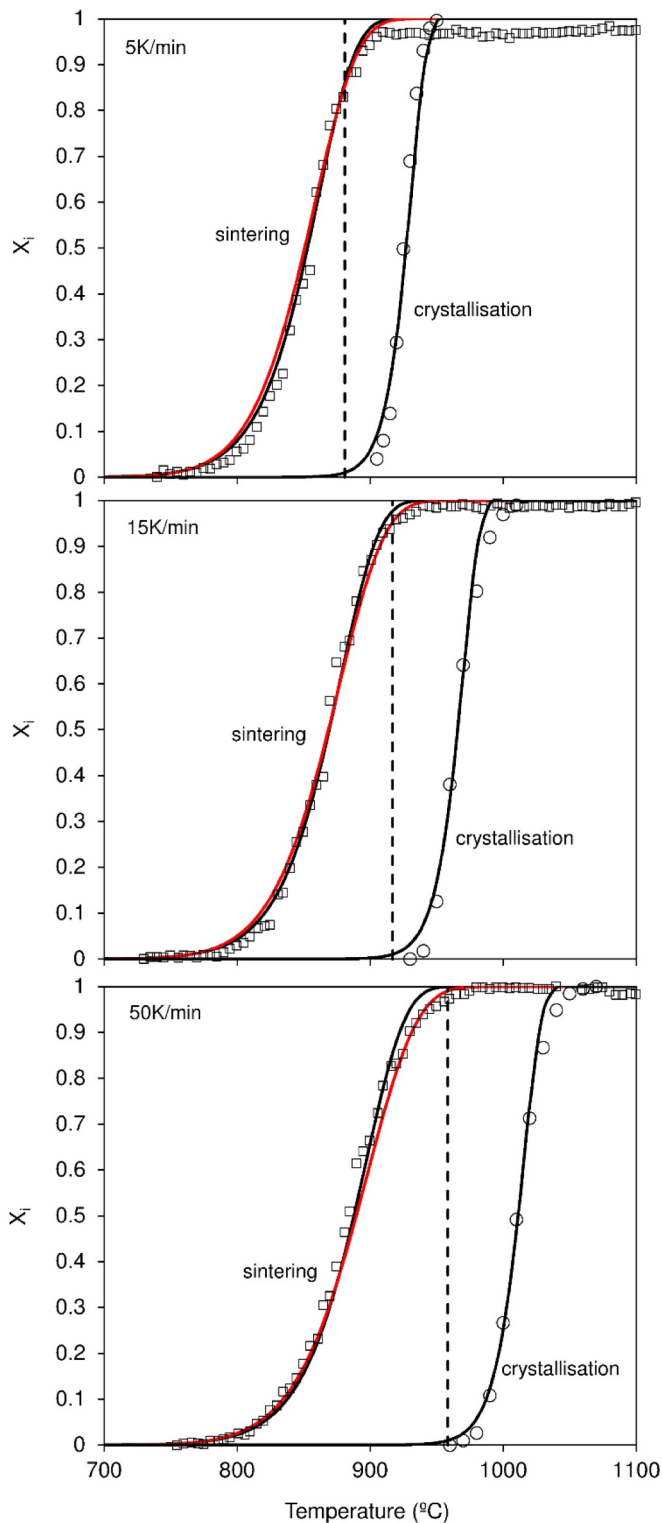
Fig. 18. Effect of heating rate, a, on sintering and crystallisation. The squares and circles are experimental data on sintering and crystallisation, respectively. The crystallisation curve was calculated from Eq. (12) with $n_C = 3$, $E_C = 330$ KJ/mol, and $A_C = 4.7 \cdot 10^{11}$ s^{-1}. The black sintering curve was calculated from Eq. (12) with $n_S = 0.56$, $E_S = 700$ KJ/mol, and $A_S = 8.6 \cdot 10^{29}$ s^{-1}. The red sintering curve was calculated from Eq. (14) with $n_S = 0.56$, $B = 7100$ K, $T_0 = 600$ K, and $A^* = 9.5 \cdot 10^{10}$ s^{-1}. The dashed line is the temperature at which $X_C = 0.01$. (For interpretation of the references to color in this figure legend, the reader is referred to the web version of this article.)
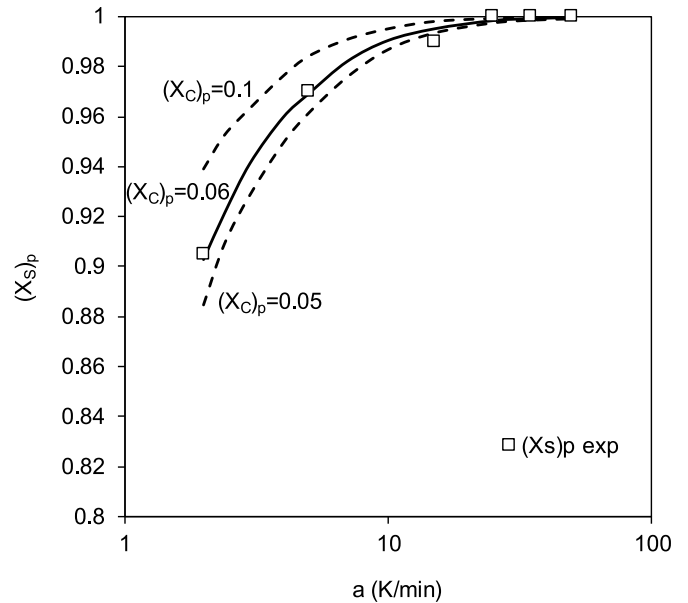

Fig. 19. Curves: $(X_S)_p$ vs a, at $(X_C)_p = 0.05$ and $(X_C)_p = 0.1$ (dashed lines) and $(X_C)_p = 0.06$ (solid line). The squares are the experimental values $(X_S)_p$ at which sintering halted.

crystallisation, $(X_C)_p$, increased. The plot also includes the experimental values of the degree of sintering at which glaze densification halted, $(X_S)_p$. These results fitted very well to the curve (solid line): $(X_S)_p$ vs a, at $(X_C)_p = 0.06$. This means that glaze densification halted when the glaze degree of crystallisation was 6%. It may further be observed that, at high heating rates, $a \geq 25$ K/min, sintering had already been completed before this critical degree of crystallisation was reached. These results are consistent with those reported in the literature [23,24,32,33], which indicate that, for materials in which sintering and crystallisation partly overlapped, as the heating rate, a, decreased, glaze densification by surface crystallisation halted at a lower degree of sintering, i.e. at higher porosities.

4. Conclusions

The present study examines the microstructural development, stemming from sintering and crystallisation, during thermal treatment at a heating rate of 15 K/min of a SiO_2–Al_2O_3–RO (R = Ca, Mg, Sr) glass-ceramic glaze. Anorthoclase and diopside phase devitrification was verified to begin before sintering had been completed. DTA and SEM–EDS analysis showed that surface crystallisation of these phases was involved and that phase size and shape depended on starting frit particle size. In the range of temperatures from anorthoclase and diopside crystallisation onset to, essentially, diopside melting temperature, crystal size, as well as intergranular and induced crystallisation pore size, increased practically without modifying specimen shrinkage. At temperatures above melting temperature, 1160 °C, only anorthoclase crystals were observed, which increased in size and in Al_2O_3 and SrO contents as temperature rose.

The DTA results at different heating rates were used to determine the values of the crystallisation activation energy and the Avrami index by different methods. The results obtained were very similar in every case. The resulting Avrami index, $n_C = 3$, corresponded to surface crystallisation of very fine particles. The JMAK model, with $n_C = 3$ and activation energy of $E_C = 330$KJ/mol, appropriately described the effect of the heating rate on the frit crystallisation process.

Sintering kinetics were determined from HSM tests at different heating rates. Sintering activation energy displayed the same trend as

viscous flow activation energy. The JMAK model also appropriately described glass-ceramic glaze sintering, but with an Avrami index below 1, namely $n_S = 0.56$, as has been obtained for other materials, and an activation energy of $E_S = 700$ KJ/mol. Assuming the effect of temperature on the rate constant to be the same as that of this variable on the inverse of glass matrix viscosity, a new model was developed that only required a single fitting parameter. The new model also yielded very good results.

It was verified that, as the heating rate increased, the crystallisation and sintering degree of overlap decreased. At high heating rates, $a \geq 25$ K/min, crystallisation took place when sintering had already ended. From the developed models, it was estimated that the degree of crystallisation required to halt sintering was about 6%.

CRediT authorship contribution statement

J.L. Amorós: Conceptualization, Methodology, Formal analysis, Writing - original draft, Writing - review & editing, Supervision. **E. Blasco:** Conceptualization, Methodology, Formal analysis, Writing - original draft, Writing - review & editing, Visualization, Supervision. **A. Moreno:** Conceptualization, Resources, Data curation, Supervision, Project administration, Funding acquisition. **N. Marín:** Software, Validation, Investigation, Data curation. **C. Feliu:** Resources, Data curation, Supervision, Project administration, Funding acquisition.

Declaration of Competing Interest

The authors declare that they have no known competing financial interests or personal relationships that could have appeared to influence the work reported in this paper.

Acknowledgements

References

[1] W.E. Matthes, Keramische Glasuren, Grundlagen, Eigenschaften, Rezepte, Anwendung. Augustus Verlag, 1997.

[2] S. Stefanov, S. Batschwarov, Keramik-Glasuren: Ceramic glazes, Wiesbaden and Berlin, Bauverlag GmbH, 1988.

[3] P. Murray, J. White, Kinetics of the thermal dehydration of clays. Part IV. Interpretation of the differential thermal analysis of the clay minerals, Trans. Br. Ceram. Soc. 54 (1995) 204–264.

[4] T. Akahira, T. Sunose, Method of determining activation deterioration constant of electrical insulating materials, Res Rep Chiba Inst Technol (Sci Technol) 16 (1971) 22–31.

[5] H.E. Kissinger, Reaction kinetics in differential thermal analysis, Anal. Chem. 29 (1957) 1702–1706.

[6] S. Vyazovkin, A.K. Burnham, J.M. Criado, L.A. Pérez-Maqueda, C. Popescu, N. Sbirrazzuoli, ICTAC Kinetics Committee recommendations for performing kinetic computations on thermal analysis data, Thermochim. Acta 520 (1–2) (2011) 1–19.

[7] D. Chen, X. Gao, D. Dollimore, A generalized form of the Kissinger equation, Thermochim. Acta. 215 (1993) 109–117.

[8] T.J.W. De Bruijn, W.A. De Jong, P.J. Van Den Berg, Kinetic parameters in Avrami–Erofeev type reactions from isothermal and non-isothermal experiments, Thermochim. Acta. 45 (3) (1981) 315–325.

[9] J. Shi, F. He, J. Xie, X. Liu, H. Yang, Kinetic analysis of crystallization in Li$_2$O-Al$_2$O$_3$-SiO$_2$-B$_2$O3-BaO glass-ceramics, J. Non-Cryst. Solids. 491 (2018) 106–113.

[10] R. Svoboda, J. Málek, Interpretation of crystallization kinetics results provided by DSC, Thermochim. Acta 526 (2011) 237–251.

[11] J. Málek, Kinetic analysis of crystallization processes in amorphous materials, Thermochim. Acta. 355 (2000) 239–253.

[12] M. Avrami, Kinetics of phase change. I. General theory, J. Chem. Phys. 12 (7) (1939) 1103–1112.

[13] M. Avrami, Kinetics of phase change. II. Transformation–time relations for random distribution of nuclei, J. Chem. Phys. 2 (8) (1940) 212–224.

[14] J.L. Amorós, E. Blasco, A. Moreno, E. Zumaquero, C. Feliu, Non-isothermal sintering of powdered vitrified composites. A kinetic model, Mater. Lett. 236 (2019) 236–239.

[15] J.L. Amorós, Towards rational design of porcelain tile glazes, Adv. Sci. Technol 92 (2014) 138–147.

[16] J.L. Amorós, E. Blasco, A. Moreno, M.P. Gómez-Tena, Sintering of raw glazes for floor and porcelain tiles: a non-isothermal kinetic model, Ceram. Int. 42 (2016) 16169–16179.

[17] M.J. Pascual, C. Lara, A. Durán, Non-isothermal crystallisation kinetics of devitrifying RO-BaO-SiO2 (R = Mg, Zn) glasses, Phys. Chem. Glasses: Eur. J. Glass Sci. Technol., Part B. 47 (5) (2006) 572–581.

[18] C.S. Ray, W. Huang, D.E. Day, Crystallization kinetics of a lithia silica glass: Effect of sample characteristics and thermal analysis measurement techniques, J. Am. Ceram. Soc. 74 (1) (1991) 60–66.

[19] T. Ozawa, A modified method for kinetic analysis of thermoanalytical data, J. Therm. Anal. 9 (3) (1976) 369–373.

[20] J.A. Augis, J.E. Bennett, Calculation of the Avrami parameters for heterogeneous solid state reactions using a modification of the Kissinger method, J. Therm. Anal. 2 (13) (1978) 283–292.

[21] J.M. Fernández-Navarro, El vidrio, CSIC, Madrid, 1991.

[22] M.J. Pascual, M.O. Prado, A new method for determining fixed viscosity points of molten borosilicate glasses, Phys. Chem. Glasses. 46 (5) (2005) 512–520.

[23] J.L. Amorós, E. Blasco, A. Moreno, M.P. Gómez-Tena, C. Feliu, Non-isothermal sinter-crystallization of satin glazes: a kinetic model, Ceram. Int. 44 (2018) 7780–7787.

[24] A. Karamanov, M. Pelino, Sinter-crystallisation in the diopside–albite system: Part I. Formation of induced crystallisation porosity, J. Eur. Ceram. Soc. 26 (2006) 2511–2517.

[25] A. Karamanov, M. Pelino, Sinter-crystallization in the diopside–albite system: Part II. Kinetics of crystallization and sintering, J. Eur. Ceram. Soc. 26 (2006) 2519–2526.

[26] A. Karamanov, I. Avramov, L. Arrizza, R. Pascova, I. Gutzow, Variation of Avrami parameter during non-isothermal surface crystallization of glass powders with different sizes, J. Non-Cryst. Solids. 358 (2012) 1486–1490.

[27] R. Müller, The influence of grain size on the overall kinetics of surface-induced glass crystallization, J. Therm. Anal. 35 (3) (1989) 823–835.

[28] I. Gutzow, R. Pascova, A. Karamanov, The kinetics of surface induced sinter-crystallization and the formation of glass-ceramic materials, J. Mater. Sci. 33 (1998) 5265–5273.

[29] R. Müller, On the kinetics of sintering and crystallization of glass powders, Glastech. Ber. -Glass Sci, Technol. 67C (1994) 93–98.

[30] A. Karamanov, B. Dzhantov, M. Paganelli, D. Sighinolfi, Glass transition temperature and activation energy of sintering by optical dilatometry, Thermochim. Acta 553 (2013) 1–7.

[31] E. Blasco, Sinterización de compactos de vidrio y composites vidrio-circón. Mecanismo y cinética del proceso, Universitat Jaume I. Department of Chemical Engineering, 2017.

[32] A. Karamanov, M. Pelino, A. Hreglich, Sintered glass-ceramics from municipal solid waste-incinerator fly ashes–part I: the influence of the heating rate on the sinter-crystallisation, J. Eur. Ceram. Soc. 23 (2003) 827–832.

[33] M.O. Prado, M.L.F. Nascimento, E.D. Zanotto, On the sinterability of crystallizing glass powders, J. Non-Cryst. Solids. 354 (2008) 4589–4597.